On the Intraseasonal Oceanic Processes Constrained by Data Assimilation: A Case Study of the Tropical Pacific

B. ROHITH,[a,b,d] FLORENT GASPARIN,[a] GIOVANNI RUGGIERO,[b] ELISABETH REMY,[b] AND SOPHIE CRAVATTE[a,c]

[a] *Université de Toulouse, LEGOS (CNES/CNRS/IRD/UT3), Toulouse, France*
[b] *Mercator Ocean International, Toulouse, France*
[c] *IRD Center, Nouméa, New Caledonia*
[d] *Indian National Center for Ocean Information Services, Hyderabad, India*

(Manuscript received 8 February 2024, in final form 10 October 2024, accepted 17 December 2024)

ABSTRACT: This study investigates the ability of a global ocean reanalysis at 1/12° horizontal resolution, GLORYS12, to represent oceanic processes at intraseasonal and higher-frequency scales. GLORYS12, which includes data assimilation of satellite and multi-instrument in situ observations, is compared to a twin-free simulation (with no assimilation) in the tropical Pacific Ocean. Spectral analyses show that data assimilation improves the realism of sea surface height intraseasonal variability in the entire tropical Pacific Ocean, in both amplitude and phase, with an increase in the amplitude of more than 50% for the 20–90-day band and up to 15% for the 2–20-day band. The improvement is largest along the 5°N/S latitudes, where the magnitude of tropical instability waves is maximum, but is limited along the equator where steric height variability is dominated by intraseasonal oceanic Kelvin waves, already well represented in the free simulation. Wavenumber–frequency spectra show that data assimilation constraint improves both the spatial and temporal scales of intraseasonal waves and their timing. Data assimilation impacts the realism of oceanic simulations in two ways. By modifying the background oceanic stratification, it corrects the phase speed of westward-propagating waves. It is also shown that the intraseasonal component of analysis increments (data assimilation corrections applied) is dynamically consistent and exhibits clear intraseasonal propagation. By demonstrating the benefits of data assimilation for intraseasonal processes in the tropical Pacific Ocean, this study highlights the high value of both in situ and satellite observations to constrain ocean models in a wide range of time scales.

KEYWORDS: Oceanic waves; Planetary waves; Data assimilation; Ocean models; Intraseasonal variability

1. Introduction

Oceanic reanalyses are very powerful tools to synthesize ocean observations using numerical ocean models. These gridded products, dynamically constrained via data assimilation (DA), add value through their consistent integration of information from diverse sources, combining satellite and in situ observations. They are widely used by a diverse range of end users, such as researchers, climate change services, and various ocean enterprise-related business actors, as the information they provide can be more easily and effectively accessed.

Several operational centers provide routine oceanic reanalyses by assimilating the various available observations and trying to make the best use of them. One would ideally expect the reanalyses to mimic the real ocean variability at all relevant spatial and temporal scales. This is far from reality, as the reliability of ocean reanalyses strongly depends (i) on the numerical model, on its biases, and on the physical processes it is able to simulate; (ii) on the dataset available, whose temporal sampling and/or spatial sampling are limited, and (iii) on the DA methods that might smooth or lose important information provided by the data. Currently, the large biases in the ocean dynamics of numerical models and the approximations made by the assimilation techniques clearly hamper the influence of observations in operational systems (Fujii et al. 2019). Improving the data assimilation systems for maximizing the utility of ocean observations is an ongoing effort to improve the cost-effectiveness of the Global Ocean Observing System and increase the benefit to societies (Storto et al. 2019).

In the tropical Pacific Ocean, significant oceanic variability is found at various time scales: at seasonal and interannual time scales, in link with El Niño–Southern Oscillation (ENSO), the dominant mode of climate variability; at intraseasonal time scales, in response to intraseasonal atmospheric variability [such as the Madden–Julian oscillation (MJO)], or associated with features such as tropical instability waves or mesoscale eddies. Variability is also observed at higher frequencies: at diurnal, tidal, and inertial time scales. Observations available come from a combination of various platforms, each having very diverse temporal and spatial sampling and each bringing value for constraining the ocean state (Cravatte et al. 2016; Smith et al. 2019). For example, satellite systems provide global spatial and temporal observational coverage of the surface. Argo float profiles provide high vertical resolution of temperature and salinity but are not adequate to sample the short time and spatial scales (Gasparin et al. 2023). On

---

Denotes content that is immediately available upon publication as open access.

Supplemental information related to this paper is available at the Journals Online website: https://doi.org/10.1175/MWR-D-24-0027.s1.

Corresponding author: B. Rohith, rohith.b@incois.gov.in

DOI: 10.1175/MWR-D-24-0027.1

the contrary, the TAO/TRITON moored array provides unique information on the high-frequency variability, yet these fixed-point measurements exhibit a rather wide spacing (located every 10°–15° in longitude and 2°–5° in latitude), and their vertical sampling is too limited to constrain either the mixed layer or the thermocline.

While these observations constituting the Tropical Pacific Observing System (TPOS) are all ingested via the DA system, their utilization and effective influence on ocean state estimates in reanalyses remains poorly understood. A necessary preliminary step to improve the way these data are assimilated is to improve our understanding of their impacts on various time and spatial scale processes in reanalysis products. As a first step toward that goal, this study aims to characterize the intraseasonal time and spatial scales that can be (and that are) effectively constrained by data assimilation in one system, the Mercator Ocean reanalysis system. Recent studies clearly highlighted the benefit of data assimilation in controlling the low-frequency variability of the ocean (e.g., Gasparin et al. 2018; Lellouche et al. 2021). However, little is known about the benefit of DA for higher-frequency processes. Some processes sampled by the observations (such as internal tides and submesoscale) are not simulated in the model and cannot be constrained by DA and should be filtered from the information ingested. Others, such as mesoscale eddies, tropical instability waves (TIWs), and intraseasonal equatorial waves, are important features that can be simulated and should ideally be constrained to respond to the increasing demand for higher temporal and spatial resolution by end users (e.g., Le Traon et al. 2019; Storto et al. 2019).

This study focuses on the high-frequency band (<90 days) and aims to

- Characterize the time and spatial scales sampled by the observing system (OS) that can be (and that are) effectively constrained by DA in the Mercator Ocean System
- Evaluate the improvements in intraseasonal and high-frequency process realism due to data assimilation
- Understand how data assimilation may modify intraseasonal wave characteristics

The paper is organized as follows. Section 2 describes the different simulations and data used, as well as the main evaluation metrics. Section 3 investigates the time and spatial scales that are captured by the observations, in the GLORYS12 reanalysis simulation and its free version (without DA). Section 4 evaluates the improvement in intraseasonal variability due to DA, and section 5 investigates the process by which DA constrains the intraseasonal wave characteristics. We believe that these initial steps will help to identify the specific time and spatial scales which are dynamically constrained by assimilation and ultimately will lead to improvement in DA systems.

2. Datasets and methodology

a. *Ocean reanalysis simulations, assimilation experiments, and validation datasets*

1) GLORYS12 REANALYSIS SIMULATIONS

In the framework of the Copernicus Marine Service, Mercator Ocean delivers the GLORYS12 global eddy-resolving oceanic reanalysis, covering the 1993–present altimetry period (Lellouche et al. 2021). The ocean model component is based on version 3.1 of the NEMO model in its ORCA12 configuration (1/12° ORCA grid type). There are 50 vertical levels from the surface to the bottom, including 22 levels within the upper 100 m, with 1-m resolution near the surface and 450-m resolution at the bottom. The atmospheric forcing fields are obtained from the European Centre for Medium-Range Weather Forecasts interim reanalysis (ERA-Interim) at 3-h resolution (Dee et al. 2011). GLORYS12 was initialized using temperature and salinity (T/S) profiles from the EN4 monthly gridded climatology (Good et al. 2013), starting in December 1991. More details concerning the parameterization of the terms included in the momentum, heat, and freshwater balances (i.e., advection, diffusion, mixing, or surface flux) can be found in Lellouche et al. (2018).

Observations jointly assimilated to estimate corrections applied to the GLORYS12 model trajectory include reprocessed along-track satellite altimeter missions sea level anomalies (SLAs) from the Copernicus Marine Service (Pujol et al. 2016), satellite AVHRR sea surface temperature (SST) from NOAA, sea ice concentration, and in situ temperature and salinity vertical profiles delayed-mode quality-controlled Coriolis Ocean Dataset for Reanalysis (CORA) database (Cabanes et al. 2013; Szekely et al. 2019), including various in situ platforms [XBT, Argo floats, conductivity–temperature–depth (CTD) casts, tropical moored array, gliders, and sea mammals].

Data assimilation techniques are detailed in Lellouche et al. (2013, 2018) and include two steps: (i) a 3D-Var correction for the slowly evolving large-scale error of the model temperature and salinity, based on in situ T/S profiles over the last month, and (ii) a reduced-order Kalman filter derived from a singular evolutive extended Kalman filter [SEEK; Brasseur and Verron (2006)], with a three-dimensional multivariate background error covariance matrix and a 7-day assimilation cycle. This multivariate procedure considers satellite and in situ observations and presumably corrects patterns at smaller spatial and temporal scales (mesoscale). The method produces corrections for temperature, salinity, sea surface height, horizontal velocities, and sea ice concentration. In parallel, a twin simulation using the model configuration, but without DA, has been performed starting from the same initial condition as GLORYS12 for the 1993–2016 period. The intercomparison between the two simulations will allow quantifying the impact of DA on the simulation of physical processes.

In the following, the simulation without DA is called “freerun” while GLORYS12 is referred to “analysis.” We use hourly and daily averaged fields of SLA (anomalies from the 2004–16 period) and computed surface dynamic height relative to 500 m based on daily averaged temperature and salinity fields. Model fields have been resampled onto a $\frac{1}{4} \times \frac{1}{4}$ degree grid, to be comparable to the satellite altimeter data, and model outputs were extracted at the nearest location for in situ TAO comparison. The surface dynamic height calculation was performed using all vertical levels available in the simulation and using only the vertical levels available on TAO moorings to ease the comparison between simulated and observed dynamic height. Data assimilation corrections

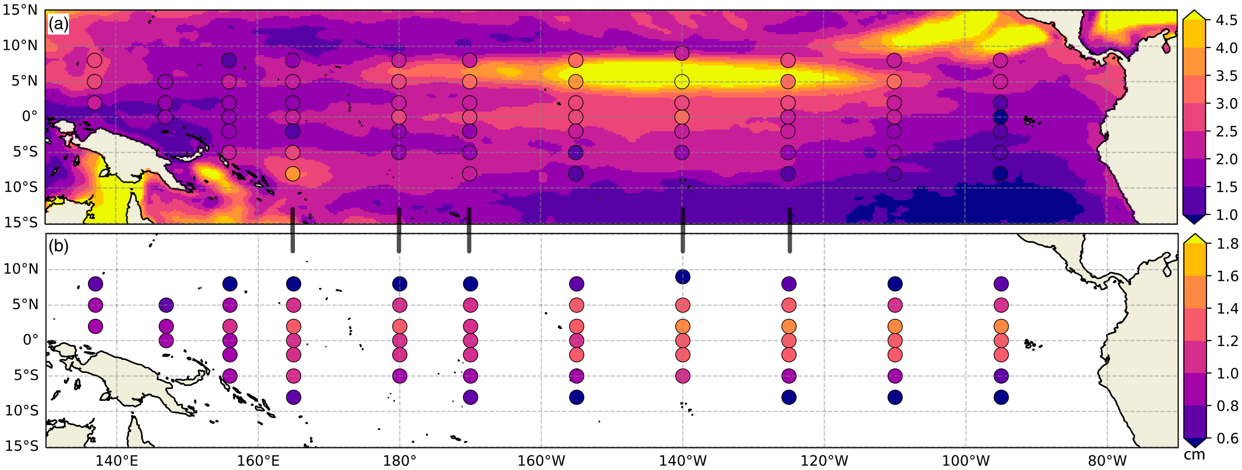

FIG. 1. STD of bandpass-filtered observed SLA and dynamic height (cm) in (a) the 20–90-day intraseasonal band and (b) the 2–20-day HF band. Shading shows SLA STD from AVISO in the upper panel, and the dots show dynamic height STD from in situ tropical moorings in both panels.

are calculated from SEEK and 3D-Var increments by linearly adding them with the weight 1 and 1/4, respectively, to account for the different assimilation windows of the SEEK and 3D-Var schemes (see Lellouche et al. 2018 for more explanation).

2) VALIDATION DATASETS

(i) Satellite altimeter

Multisatellite altimetry observations provide sea surface height over the global ocean. The SSALTO/Data Unification and Altimeter Combination System (DUACS) delayed-time level-4 sea level anomaly product consists of daily gridded fields with a horizontal resolution of 1/4°. Anomalies from the 2004–16 period have been considered here and have been downloaded from the Copernicus Marine Service catalog (http://marine.copernicus.eu).

(ii) Tropical moored buoy observations

Hourly and daily averaged surface dynamic heights relative to 500 m from the TAO/TRITON mooring array over the 1997–2022 period are also used. This array spans the tropical Pacific region (with moorings at 0°, 2°S, 2°N, 5°S, 5°N, 8°S, and 8°N) with a nominal longitudinal spacing of 15° (McPhaden et al. 1998). All data used are from nine longitudes between 156°E and 95°W (indicated in Fig. 1). Note that subsurface salinity is not systematically measured on the TAO/TRITON moorings and is estimated, when absent, based on a temperature–salinity regression using climatological data at each location and depth. This dataset has been downloaded from the TAO Project Office website (http://www.pmel.noaa.gov/tao/data_deliv/dyn.html).

b. Temporal- and spatial-scale separations

To better estimate the ability of observations to constrain the ocean state through DA, it is useful to look separately at key physical processes identified by their spatial and temporal scales and analyze if their simulation is improved with DA. To this end, we filtered the oceanic variables of interest (SLA and dynamic height) into different frequency and wavenumber bands. The various methods to isolate processes are described below.

1) ZONAL WAVENUMBER–FREQUENCY SPECTRUM

Spectral analysis is a useful tool to separate processes at various time and space scales. This can be achieved by examining the spectrum of oceanic variability in the zonal wavenumber–frequency domain (Wheeler–Kiladis diagram; Wheeler and Kiladis 1999; Roundy and Frank 2004; Farrar and Weller 2006; Farrar 2008; Farrar and Durland 2012). Here, the diagram was made using the NCAR command language available online (https://www.ncl.ucar.edu/Document/Functions/Diagnostics/wkSpaceTime.shtml; NCAR Command Language 2019). In the following, the term space–time spectrum is used for the zonal wavenumber–frequency spectrum.

Space–time spectrum of a given longitude–time section of SLA is computed using a two-dimensional (time and space) fast Fourier transform method. The longitude–time mean is removed from each longitude–time section. To adequately resolve the processes with periods up to 90 days, the time series is sliced into overlapping 1000-day segments with an overlap of 50 days, each of which is detrended and tapered to zero with a cosine-rectangular window over the first and last 12 days. Power and cross power are computed and then averaged over all segments and latitudes. This procedure results in a raw spectrum. To emphasize local maximum signals throughout the wavelength–frequency space, Wheeler and Kiladis (1999) chose to remove a background spectrum from the calculated raw spectrum. They defined the background spectrum as a smoothed version of the raw spectrum obtained by applying a 1–2–1 filter to the raw spectrum in the wavelength–frequency space. The wavenumber–frequency diagram results from the division of the raw spectrum at each point (wavenumber, frequency) by the background spectrum. For the calculations shown here, we use the 6.5°N–6.5°S latitude range;

the raw and background spectra are obtained separately from altimeter data and model simulations. Although the resulting spectra are generally similar with and without background spectrum removal, removing the background spectrum highlights the resultant anomaly of variability, which is crucial for comparing the results (Fig. 1 in the online supplemental material). Therefore, we believe it is better to keep the spectrum with the background removed.

2) COSPECTRUM ANALYSES (COHERENCE AMPLITUDE AND PHASE)

The squared coherency (called coherence amplitude here) is a measure that quantifies the degree of relationship between two signals in the frequency domain. It identifies the frequencies at which the two signals most strongly covary. It is calculated by taking the squared magnitude of the cross-spectral density between two signals and dividing it by the product of their individual power spectral densities; it ranges from 0 to 1.

Coherence phase refers to the offset or shift in the timing of one signal relative to another signal at one frequency f, often expressed in degrees or radians. It is a crucial concept when analyzing the relationships between signals in the frequency domain. Phase information provides insights into the temporal alignment or synchronization between signals at different frequencies. A phase shift of 0° means that two signals are perfectly in phase, while a phase shift of 180° indicates that they are perfectly out of phase.

Two signals of frequency f are considered highly coherent if coherence amplitude $(f) = 1$ and phase $(f) = 0$. The number of degrees of freedom (DOFs) is estimated using the following expression (Bendat and Piersol 2010, p. 89):

$$\mathrm{DOF} = 2N(\Delta T/T1 - \Delta T/T2) - 2\mathrm{D},$$

where ΔT is the sample interval, N is the sample size, and $T1$ and $T2$ are the cutoff periods in the bandpass filtering (respectively, 20 and 90 days for the intraseasonal band; 2 and 20 days for the high-frequency band; see in the following). Hence, the number of DOFs varies across the tropical moorings because the sample size N varies. As a result, the 95% confidence interval varies across the tropical moorings.

3) RADON TRANSFORMATION

Radon transformation is a mathematical technique used to estimate signal propagation speed (Challenor et al. 2001). It works by projecting a Hovmöller diagram [space (longitude/latitude) and time] onto a line at various angles ranging from 0° (aligned with the x or longitude axis) to 180° (with the y or time axis at 90°). When the line is perpendicular to the alignment of the wave crests and troughs, the projection exhibits maximum energy (i.e., maximum variance). To determine the direction of wave propagation and estimate phase speed, we identify the projection that yields the maximum variance and record the angle θ of the perpendicular to that projection.

We use this technique to compute the propagation speed of the tropical instability waves in section 4c. We applied this method for the period 2011–12 over 10° longitudinal sections from 190° to 240°E and calculated the standard deviation (STD) to obtain an error estimate for the wave speed.

3. Intraseasonal and high-frequency variability constrained by data assimilation

To focus on subseasonal oceanic variability, SLA and dynamic height time series from satellite altimeter and in situ mooring observations, respectively, are first filtered by applying a 90-day high-pass Butterworth filter. Intraseasonal and high-frequency components are then separated by applying a 20-day Butterworth filter. The 20-day separation period is chosen since time scales shorter than 20 days (i) cannot be resolved by the DUACS SLA altimetric product (which has an effective temporal resolution of 21 days in the tropical Pacific; Ballarotta et al. 2019) and (ii) can only be partially constrained by DA (since the SEEK data assimilation window is of 7 days). The high-frequency (2–20 days) variability is examined based on hourly in situ mooring observations only. The same filtering procedures are applied to model fields.

a. Processes resolved by in situ and satellite observations

Figure 1 shows the standard deviation of the bandpass-filtered SLA and dynamic height signals in the two frequency bands. In the intraseasonal band (Fig. 1a), the oceanic variability as revealed by altimetric and in situ data is very similar. In the 10°S–10°N band, the largest amplitude is seen along 5°N, corresponding to the latitude with the largest TIW SSH signals (e.g., Lyman et al. 2007). A secondary peak is visible in both altimetry and moorings along the equator. Note that the northeast and southwest tropical regions (the gap winds and Solomon Sea regions, respectively) also exhibit significant variability which has been linked to the presence of mesoscale eddies (Willett et al. 2006; Melet et al. 2010; Gourdeau et al. 2017). In the high-frequency band (Fig. 1b), the largest variability is observed along the equatorial band, with a maximum around 2° of latitude seen mostly in the eastern part of the basin and a decrease to near zero around 10° latitude. This signal can be related to the presence of equatorial inertia–gravity waves and mixed Rossby–gravity waves (Farrar and Durland 2012). Note that the high-frequency variability represents less than half the intraseasonal variability.

The ability of the observational network to resolve the meridional structure of the oceanic variability is then examined in Fig. 2, with the standard deviation of the SLA/dynamic height along five longitudinal sections at 165°E, 180°, 155°W, 140°W, and 125°W. The amplitude of the intraseasonal variability exhibits an antisymmetric pattern with a clear maximum around 5°N (Fig. 2a). Even if moorings and altimetry are broadly consistent at the mooring locations, it appears that the meridional spacing of moorings (0°, 2°, and 5°) cannot precisely resolve the peak in variability observed by altimetry (this is particularly striking at 155°W). The amplitude of the high-frequency variability (Fig. 2b) clearly shows peaks around 2° of latitude (4 times lower than the intraseasonal frequency maximum), symmetric about the equator, with a

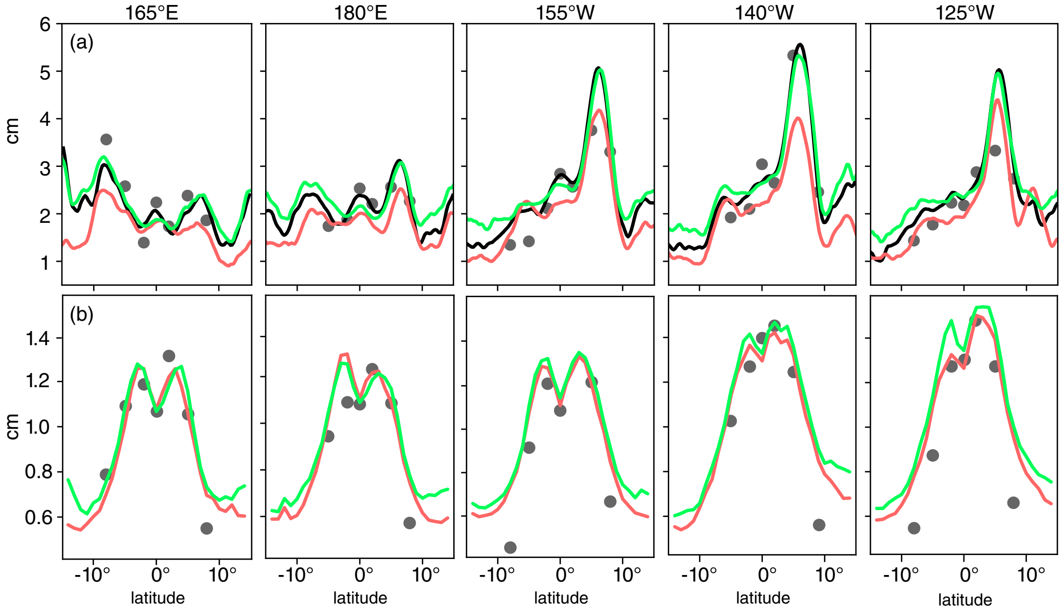

FIG. 2. STD of bandpass-filtered SLA and dynamic height in the (a) 20–90-day band and (b) 2–20-day band as a function of latitude along TAO moorings meridional sections. Dots represent dynamic height STD from moorings. Lines represent SLA STD from altimeter (black line; upper panels only), freerun (red line), and analysis (green line).

drastic decrease poleward of 2°. It should be noted that the dynamic height computed with only a few levels (such as in TAO) is similar to the one computed with the full vertical resolution of the simulations. Therefore, the limited vertical resolution of the TAO moorings is not an impediment to resolving the high-frequency processes in dynamic height (figure not shown). Note that the model may be missing some processes (e.g., internal waves) that drive errors in this calculation.

The comparison of these independent datasets at mooring locations provides good confidence in the ability of both altimetry and moorings to capture oceanic subseasonal variability. Both observing systems are strongly complementary; the global coverage of altimetry provides information on intraseasonal and longer time scales everywhere, while the high temporal resolution of fixed moorings gives access to the entire frequency spectrum but at pointwise locations. In the following, altimetry is thus chosen to be the primary observational platform to study the kinematics of intraseasonal waves, which are characterized by both space and time scales. The high-frequency variability represented in the numerical simulations will be confronted with tropical mooring observations.

b. *Impact of DA on simulated intraseasonal and high-frequency (HF) variability*

Figure 2 also compares observations with numerical simulations [freerun and analysis; see section 2a(1)] along the five meridional sections. In the intraseasonal band, the freerun correctly captures the meridional pattern of the SLA variability but underestimates its magnitude (Fig. 2a). Alternatively, the analysis can reproduce correctly the magnitude of the observed variability at all latitudes (cf. black and green curves in Fig. 2a). Averaged over the entire basin, the SLA standard deviation is 2.25 cm for the altimeter data, 1.7 cm for the freerun, and 2.25 cm for the analysis. This clearly shows that in this frequency band, DA is important to constrain the amplitude of the variability. In the high-frequency band, both numerical simulations exhibit similar amplitudes and can represent the magnitude of the observed variability (Fig. 2b), especially the symmetric peak at 2°; even if they slightly overestimate the magnitude of the variability poleward of 5°. No significant improvement in amplitude is provided by DA in the analysis in this frequency band.

As standard deviation can only identify improvements in the magnitude of the simulated variability, but not whether it varies consistently in phase with observations, coherence amplitude and phase were separately computed with respect to observations in Fig. 3. In the intraseasonal band (Figs. 3a–d), there is a considerable improvement in coherence amplitude for the analysis compared to the freerun, with values ranging from around 10% along the equator to more than 50% off equator. Largest improvements are seen in the central Pacific around 5° in both hemispheres. There, the coherence amplitude between analysis/observations is higher than 0.8, whereas it is around 0.4 between the freerun and the observations (Figs. 3a,b). Smaller improvements are seen along the equator, especially in the western part of the basin, where the coherence amplitude between the freerun and the observations is already high. This reduced impact likely results from the good skills of the freerun and/or a weak variability in this region. This will be further investigated in the next section.

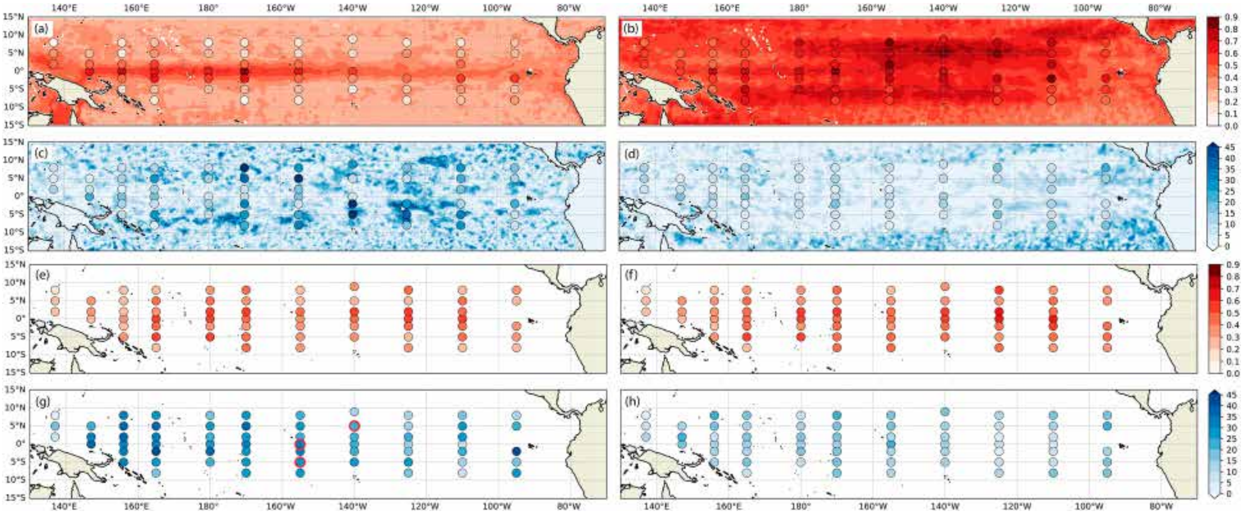

FIG. 3. Coherence amplitude (from 0 to 1) and phase (°) between observations and simulations for intraseasonal [(a)–(d) 20–90 days] and HF [(e)–(h) 2–20 days] bands for (left) the freerun and (right) the analysis run. Both altimetric SLA and mooring dynamic height are shown for the intraseasonal band, while only dynamic height is shown for the HF band. Mooring time series with gaps longer than 7 days are split into chunks. Coherence was computed for each chunk, and average coherence amplitude and phase were estimated for all the chunks having data for more than 2 years. The red color circles in (g) indicate moorings used in Fig. 4.

Clear improvements are also seen in phase. For instance, the coherence phase in the analysis is smaller than 10° in the whole 10°S–10°N band while it was closer to 15° in the freerun (Figs. 3c,d), with areas having high values.

In the high-frequency band, an overall improvement in the coherence amplitude for the analysis is also seen when compared to the freerun with values around 10% between 160° and 110°W. The most obvious improvements are seen for the coherence phase difference (Figs. 3g,h) in the western Pacific basin and along the equatorial Pacific. The coherence amplitude and phase differences decrease poleward away from 5° latitude. This clearly shows that DA improves the realism of the high-frequency processes in this 2–20-day band.

To better characterize the improvement observed in oceanic variability within each frequency band, Fig. 4 shows dynamic height coherence amplitude and phase between both the analysis and the freerun models and in situ mooring observations at three locations (red circles in Fig. 3g).

The improvement brought by DA shown in the analysis is dependent on the location of the mooring. At 155°W–0°, at the equator, a large coherence amplitude (higher than 0.8) and near-zero phase are observed between 40 and 80 days (Fig. 4, upper panels), for both the freerun and the analysis. This demonstrates that both the freerun and the analysis can resolve intraseasonal variability along the equator. In the high-frequency band (higher than 20 days), a slight improvement in phase is shown in the analysis compared to the freerun (cf. light and dark green curves in Fig. 4d), as previously illustrated in Figs. 2 and 3.

At 155°W–5°S, south of the equator, a clear improvement is observed in the analysis at intraseasonal time scales (middle panels of Fig. 4). In the analysis (dark blue), the coherence amplitude is higher than 0.5 whereas it is lower than 0.1 in the freerun (light blue). A significant improvement in phase (around 10°) is also observed in the analysis compared to the freerun (Fig. 4e, compare light and dark green curves). In the high-frequency band (2–20 days), a significant energy peak stands out around 3–5 days, but the improvement brought by DA in this frequency band remains negligible.

Finally, at 5°N, 140°W, in the TIW area, a large improvement in the analysis is seen at intraseasonal scales (Fig. 4, lower panels) across the entire 10–90-day frequency band, in terms of both coherence amplitude and phase (cf. light and dark curves in Figs. 4c,f). Here, the DA leads to a significant improvement in the realism of the ocean simulation.

To sum up, the simulation of oceanic processes at intraseasonal time scales is improved by DA, in both amplitude and phase. More surprisingly, the simulation of oceanic processes at higher frequency is also slightly improved with DA. With a 7-day assimilation window and an associated Nyquist frequency of 14 days, a large portion of the improvement at high-frequency time scales might result from a better representation of the large and lower-frequency scales. This is supported by the results from Specht et al. (2024), who highlighted that seasonality in background shear contributes significantly to the generation and modulation of instabilities at TIW fronts, as well as the associated mixing.

4. Focus on intraseasonal equatorial wave modes

Here, we adopt a space–time (zonal wavenumber–frequency) spectrum approach to relate the variability described above in different frequency bands, and different areas of the basin, to equatorial waves. This will also allow us to better identify how DA is able to constrain intraseasonal oceanic wave propagation in the tropical Pacific Ocean.

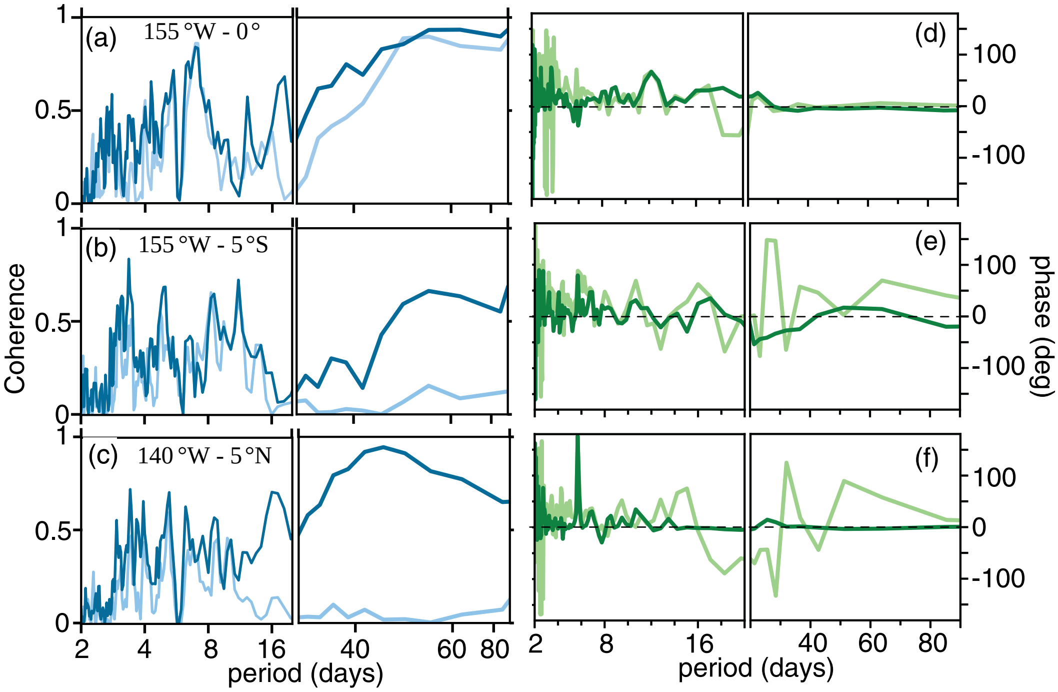

FIG. 4. (left) Coherence amplitude and (right) phase for dynamic height between mooring and simulations at (a),(d) 155°W–0°, (b),(e) 155°W–5°S, and (c),(f) 140°W–5°N. The light- and dark-colored curves are, respectively, for freerun and analysis.

a. Sea level energy distribution in wavenumber and frequency space

Wavenumber–frequency power spectra of SLA are calculated in Fig. 5 for the whole tropical Pacific belt (6.75°N–6.75°S) (see section 2b) from both observations (Fig. 5a) and numerical simulations (supplemental Figs. 1f,i). Theoretical equatorial wave dispersion curves for pressure fields inferred from the classical theory were plotted (e.g., Moore and Philander 1977; Farrar 2011). The expectations from the classical theory will help interpret SLA variations resulting from pressure fluctuations associated with the waves. Theoretical curves are only indicative; they are modified in the presence of varying currents and stratification (e.g., Chelton et al. 2003; Lyman et al. 2005).

However, the space–time spectrum from altimetry shows distribution of energy that clearly aligns with theoretical dispersion curves (Fig. 5a). The largest variability is found for positive wavenumbers, i.e., eastward-propagating signals. It aligns with the first baroclinic oceanic Kelvin waves curve. As shown previously, intraseasonal equatorial Kelvin waves exhibit higher energy in the 40–90-day band (see also Cravatte et al. 2003). Peaks are also observed along this curve at higher frequency, around 25–40-day periods, with shorter wavelengths. High energy is also found for negative wavenumbers, i.e., westward-propagating signals, aligning with the curve of the first meridional oceanic Rossby mode for periods around 30–40 days and wavelengths 10°–30°. This encompasses the TIW periods of 29.2–33.4 days and wavelengths 12.4°–15.5° (Lyman et al. 2005; Farrar 2011).

A comparison is then carried out between the observed and simulated SLA spectra (Figs. 5b,c). Positive/negative anomalies indicate an overestimation/underestimation of power for the model simulation relative to observations. The freerun spectrum also clearly aligns with the theoretical dispersion curves (Fig. 5b), with some noticeable differences with the observations. First, the power is higher along the barotropic Rossby wave dispersion curve in the simulation. Then, the discrepancies between the freerun and the observations are rather small for Kelvin waves for periods longer than 30 days, confirming that the freerun can reproduce the Kelvin wave characteristics properly at these periods, but it overestimates the energy along the Kelvin dispersion curve at higher frequency. Finally, while large positive anomalies are observed in the freerun near the TIW region (for periods of 25–42 days, wavelengths around 12°), indicating an overestimation of the energy there, the freerun underestimates the energy along the $n = 1$ meridional Rossby wave for longer wavelengths.

The space–time spectra of the analysis simulation are much closer to the observational spectra than those of the freerun (Fig. 5c), especially for the westward-propagating signals (i.e., for negative wavenumbers). A large improvement is observed near the TIW box and along the first meridional Rossby mode curve, in agreement with the large coherence improvement seen off equator in Fig. 3. The variability along the barotropic Rossby wave seems to be intensified in the analysis when compared to the freerun. Only limited improvement is seen in the high-frequency component of the Kelvin waves. This complements Fig. 3, showing that DA can broadly

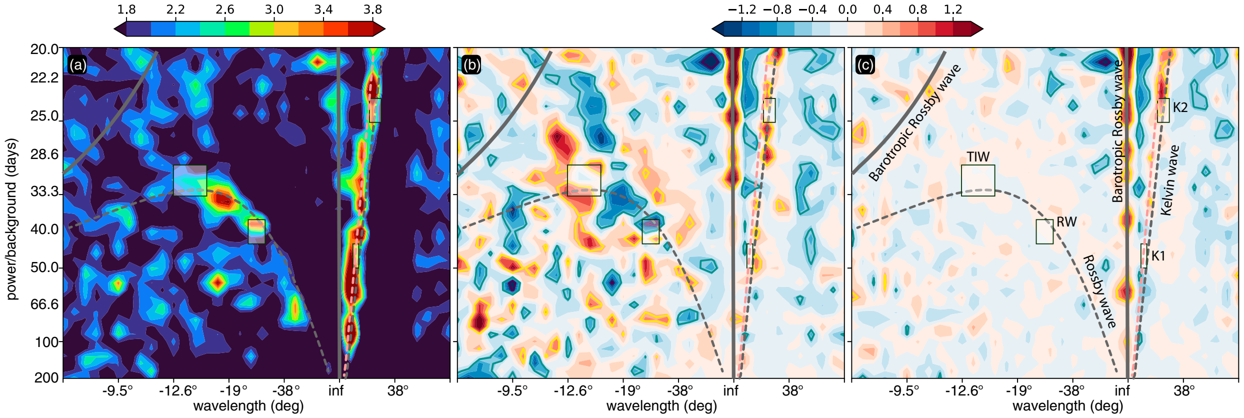

FIG. 5. Space–time spectrum of SLA averaged over 6.75°S–6.75°N for (a) altimetry, (b) freerun minus altimetry, and (c) analysis minus altimetry. For comparison, theoretical dispersion curves of the first baroclinic mode in a resting ocean are indicated by black ($c0 = 2.7$ m s^{-1}) and red ($c0 = 3.3$ m s^{-1}) for Kelvin waves, for the first ($n = 1$) meridional-mode RWs and barotropic RW ($c0 = 250$ m s^{-1}) are indicated and named in (c). Boxes represent the wavenumber–frequency bands for Kelvin waves (K1 and K2), RW $n = 1$, and TIW used in the next section.

constrain the wavelengths and the frequency content of intraseasonal oceanic waves. A more detailed investigation is done for individual equatorial waves in the next section.

b. *Coherence and phase of equatorial waves*

A coherence and cross-spectral phase analysis between numerical simulations and altimetric observations is then carried out along three meridional sections in Fig. 6 to better understand the impact of DA on Kelvin waves, Rossby waves, and TIW simulations. Kelvin wave K1 (124°; 43–50 days) has the largest amplitude in the 2°S–2°N latitude band and a consistent phase with observations for both the freerun and the analysis. The limited improvement in the analysis compared to the freerun is likely related to the good representation of these large-scale equatorial waves in the freerun. Similarly, the coherence amplitude of K2 (62°; 23–25 days) peaks at the equator for the freerun but with lower values. Moderate improvements in the analysis are seen in coherence amplitude and phase, especially at the eastern locations. While the large-scale Kelvin wave K1 is well reproduced in the freerun in amplitude and phase, the smaller-scale Kelvin wave K2 is less consistent with observations in both simulations. This lower consistency of numerical simulations with altimeter observations for K2 is likely due to the shorter period waves (around

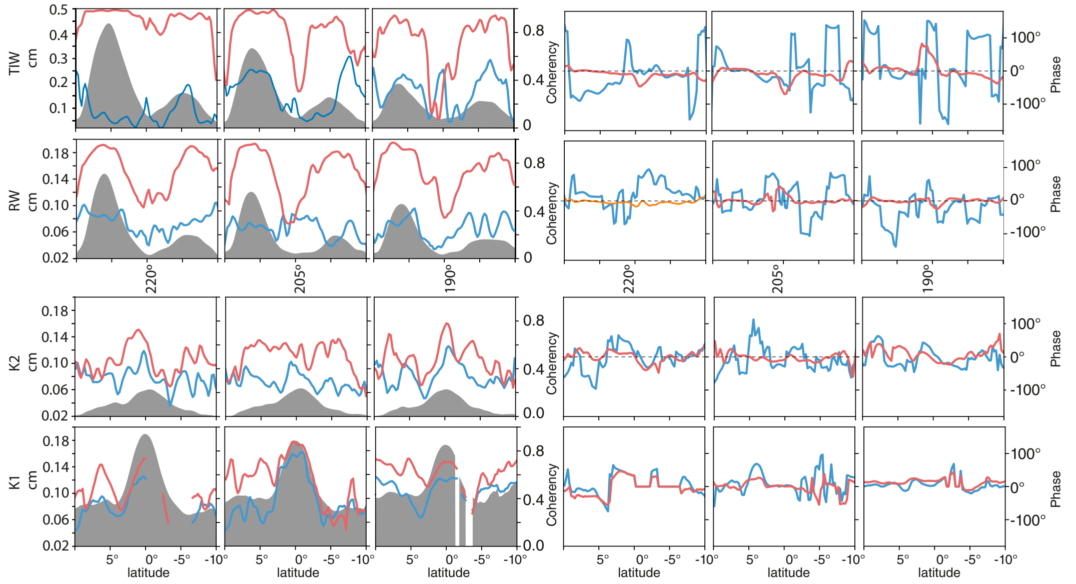

FIG. 6. (upper) Coherence amplitude and (lower) phase computed between altimetry and model simulations (freerun in blue and analysis in red) along three meridional sections (170°, 155°, 140°W) for regions identified as Kelvin waves (K1, K2), RW, and TIW in Fig. 5. Gray shading indicates the STD from the analysis run.

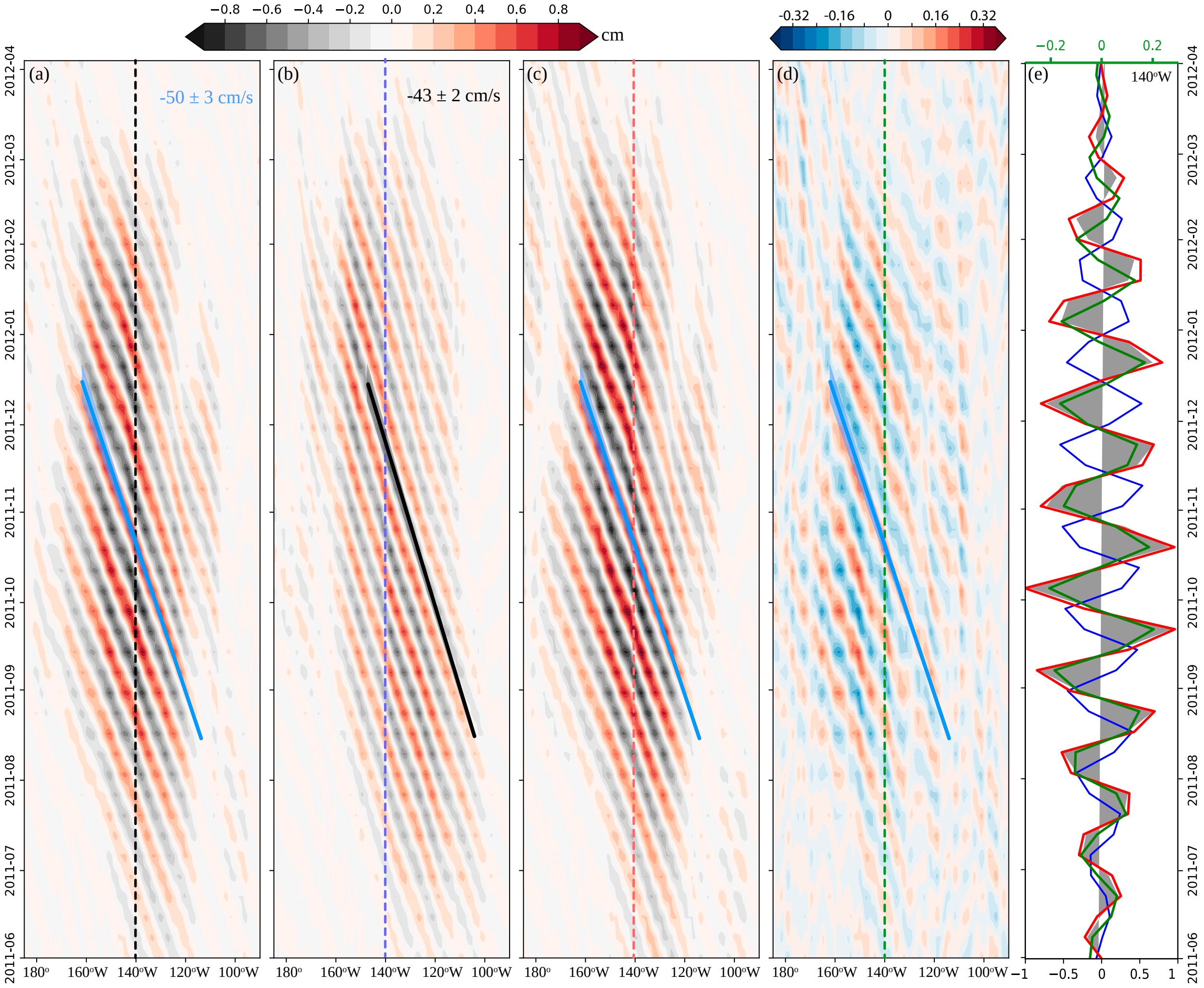

FIG. 7. (a)–(d) Time–longitude plots of SLA along 5°N latitude for the TIW box for (a) altimetry, (b) freerun, (c) analysis, and (d) DA increment. Blue lines represent the mean propagation speed from altimetry, while the black line in (b) represents the mean propagation speed from freerun (b). The shaded areas around the lines indicate the error estimates. (e) SLA time series 140°W–5°N from altimetry (shaded black), freerun (blue), analysis (red), and DA increment (green, note that *y*-axis labels are in green).

24 days), which constitutes a lower bound for the scales represented by altimeter observations and constrained by DA (see section 2).

Two regions in the space–time spectrum are used to define westward-propagating Rossby waves (RWs) (22°–28°; 37–43 days) and TIW (12.4°–15.5°; 29.2–33.4 days). These westward-propagating waves are characterized by an SLA maximum around 5°N and a second maximum at 5°S. Note that the amplitude of TIWs is greater than that of RW. The low coherence values associated with large phase difference demonstrate that the freerun is not able to sufficiently reproduce the phasing of these westward-propagating waves. A significant improvement is seen for the analysis simulation in both coherence amplitude and phase for intraseasonal Rossby waves and TIW. Maximum coherence of more than 0.8 and a phase difference close to zero (especially outside the equatorial band) confirm that DA constrains these waves in both amplitude and timing.

c. *Propagation speed of equatorial waves*

To better understand how DA improves numerical simulations and constrains the amplitude and timing of equatorial waves, we now investigate propagation speeds of SLA and analysis increments. These correspond to the corrections applied to the forecast model (Lellouche et al. 2018, 2021); they are calculated by adding the two increments of SLA from the 3D-Var and the SEEK corrections (see section 2). Figure 7 shows time–longitude plots of filtered SLA in the TIW box along 5°N latitude from observations and numerical simulations for the 2011–12 period. The wave speeds and associated errors are estimated using radon transformation [see section 2b(3)]. Observed TIWs propagate westward with a phase speed of around 50 ± 3 cm s^{-1} (Fig. 7a). Compared to observations, TIWs in the freerun propagate westward at a lower speed of 43 ± 2 cm s^{-1} (Fig. 7b), explaining why the phase difference increases toward the west. The analysis consistently represents the

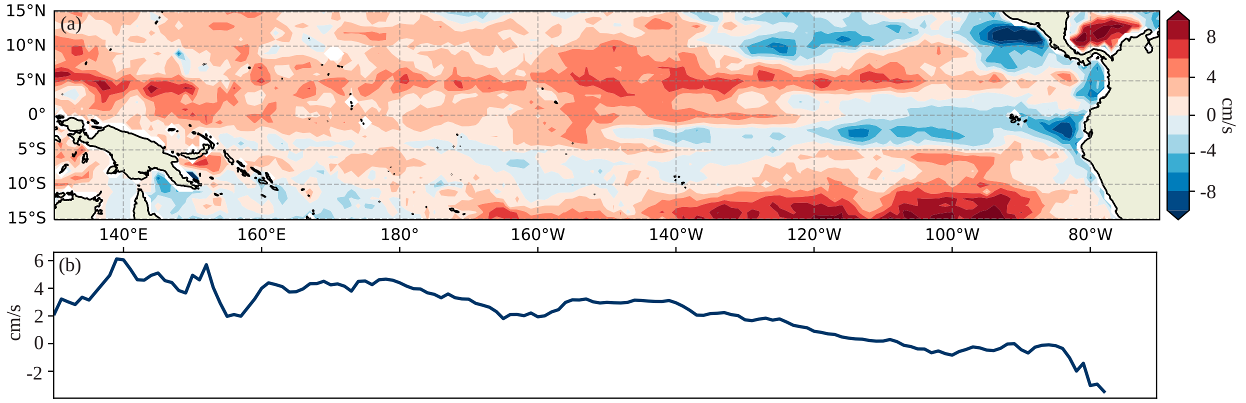

FIG. 8. (a) Mean difference in the first baroclinic gravity wave speed between analysis simulation and freerun computed from daily *T* and *S* fields for 2004–16. (b) Meridional average of (a) between 15°S and 15°N.

magnitude and phase of TIW, propagating westward with a phase speed similar to the observations (Fig. 7c).

There are two ways by which DA may improve the TIWs amplitude and propagation speed realism. The first is indirect: DA modifies the background conditions, in particular the mean stratification that in turn modifies TIW propagation. DA increments can also directly play a role in improving the TIW propagation speed, by forcing faster propagation of the anomalies. We will show below that both effects do contribute.

First, to explore the impact of a change in the oceanic mean stratification due to DA on oceanic wave propagation, the time average (2004–16) first baroclinic gravity wave speed was computed from both model simulations (supplemental Fig. 3). The theoretical difference in phase speed between the analysis and the freerun is shown in Fig. 8a. All along the equator except in the eastern Pacific region, and along 5°N, the first baroclinic gravity wave speed is larger in the analysis than in the freerun by 2–10 cm s^{-1}. Therefore, DA clearly has an indirect effect: Because of a more realistic mean oceanic stratification, the equatorial wave phase speeds are modified and more realistic.

To further disentangle the direct and indirect effects of DA in improving TIW propagation, an intermediate simulation having only a large-scale T/S correction (ONLYBIAS, no assimilation of SLA) was compared with the freerun and observations (supplemental Fig. 2). From supplemental Fig. 2, it is evident that the ONLYBIAS simulation (supplemental Fig. 2c) improves the TIW amplitude east of 130°W and the TIW phase speed but fails to accurately represent TIW propagation speeds when compared to the observation (SLA from AVISO; supplemental Fig. 2a). This suggests that correcting the background T/S structure alone, by a large-scale correction without assimilation of SLA–SST, does not suffice to constrain TIW propagation phase speed.

On the contrary, the time–longitude diagram shown in Fig. 7d reveals that DA increments exhibit a westward propagation with the correct phase speed confirming their important role in constraining these intraseasonal processes. The space–time spectrum of SLA increments shows high energy levels occurring throughout the westward-propagating quarter, confirming the importance of local increments in modulating the wave propagation. There is also large energy at the basin scale, pointing out that local increments force fast-propagating waves into the system (Fig. 5).

In conclusion, our results suggest that DA assimilation improves the large-scale background oceanic structure, contributing to a better simulation of the wave characteristics. In addition, DA increments also directly constrain the intraseasonal features' timing by forcing a faster propagation. Our results also suggest that SLA assimilation is key for constraining the TIW propagation. It is however not possible to conclude on the relative importance of both direct and indirect effects.

5. Discussion and conclusions

The main goal of this study was to evaluate the impact of data assimilation in constraining simulated oceanic processes in the tropical Pacific Ocean focusing on the high-frequency band (2–20 days) and the intraseasonal band (20–90 days). The first objective was to better understand the physical processes and associated time and spatial scales that the observations should possibly be able to constrain in ocean models based on the analysis of sea level anomaly and dynamic height provided by altimetry and tropical moorings, respectively. At intraseasonal time scales, both datasets show that the largest variability is found along 5°N, associated with intraseasonal Rossby waves and TIWs, and along the equator, associated with equatorial intraseasonal Kelvin waves. At higher frequency, the largest variability in the equatorial band corresponding to inertial–gravity waves is only seen on moorings. These sampling-dependent observation datasets are therefore complementary—which is essential to provide a broad range of information on oceanic processes associated with different temporal and spatial scales. The global coverage of altimetry deduced from several satellites can capture spatial and temporal scales typical of tropical waves, but not less than 20 days and 200 km (Ballarotta et al. 2019), while tropical moorings can capture the full time spectrum, but the separation distance of moorings (10°–15°) limits the representation to very large spatial scales (Kessler et al. 1996). Determining the potential importance of an observing system in operational systems therefore requires detailed knowledge of the ability of the observing system to capture temporal and spatial scales.

As a second objective, the comparison of two numerical simulations, with and without data assimilation, with these two datasets highlights that DA impacts are strongly dependent on oceanic processes. For instance, DA greatly improves the realism of Rossby waves and TIWs along 5° latitude, in terms of both amplitude and phase, but less for Kelvin waves along the equator. It is noteworthy that the limited gain of DA on Kelvin waves may reflect a different behavior depending on higher-frequency (23–25 days) or lower-frequency (43–50 days) Kelvin waves. Higher-frequency Kelvin waves—not well represented in the simulations—are at the lower bound of the DA constraint determined by DA techniques, i.e., 7-day assimilation window (Lellouche et al. 2018). In contrast, lower-frequency Kelvin waves—having higher amplitude and constrained by large-scale equatorial winds—are well represented in the free-run simulation. This demonstrates that DA impact is thus dependent on scales that observations can capture, but also on scales that DA can constrain (depending on DA methods), and on model skills, depending on the accuracy of modeled processes and atmospheric forcing.

Another objective was to identify how DA could improve the representation of intraseasonal variability. DA increments, spatially and temporally filtered as TIWs, are dynamically consistent and illustrate the clear impact of local DA on the striking improvement of westward-propagating intraseasonal waves. In addition to clear local effects, DA also modulates the mean stratification which in turn may modify intraseasonal variability. This is also illustrated by looking at the moderate improvement of around 10% of the high-frequency variability (2–20-day period) due to DA. Spectral coherence and phase analyses have shown that this improvement is mainly due to a better phasing of processes in the 15–20-day band. Since DA uses a 7-day assimilation window, the DA system should not be able to fully use the information brought by observations in this frequency band. Therefore, we hypothesize that a better representation of large-scale structures results in a better initialization and representation of high-frequency processes (Martin et al. 2015). The present work thus suggests that DA has direct and indirect impacts on intraseasonal and higher-frequency processes. It directly constrains the location and timing of intraseasonal waves based on the assimilation of observations that capture intraseasonal signals, but also it modifies large-scale conditions, which allows a more realistic initialization of intraseasonal and higher-frequency processes. Our results suggest that both effects are important, even if it was not possible to quantify their relative importance.

These conclusions have been obtained for the Mercator operational system, which assimilates both temperature/salinity profiles and SLA increments. Given the differences in operational systems in terms of assimilation procedures, data assimilated, and resolution, it is not straightforward to directly extend these conclusions to other operational systems. Yet we can expect that systems assimilating the same observations should be able to improve intraseasonal variability as well. The extent of the improvement will be of course dependent on the model and the assimilation system. However, systems that assimilate only T/S profiles might not observe the same level of improvement in simulating TIWs, as SLA increments play a crucial role. Most studies investigating the contribution of ocean observations on data assimilation, such as Gasparin et al. (2023), are based on 1/4° systems and have highlighted the added value of altimetry for intraseasonal scales. This suggests that our findings could be relevant to other 1/4° reanalysis systems, particularly in their ability to resolve TIWs. We hope our study will stimulate similar diagnostic efforts in other oceanic or coupled reanalysis systems to better understand the role of different observations in constraining physical processes across various temporal and spatial scales.

This study demonstrates the difficulty in determining DA impacts and, more generally, the effects of observing systems on operational systems. The problem becomes even more complex when the impact of a component of the observing system needs to be assessed since all components of the integrated observing system are conjointly used for the assimilation with specific choices in DA methods. Important work has been done with observing system simulation experiments, but it often restrains the assessment to the direct impact as indirect impact is more difficult to assess. Quantifying the impact of observations on operational systems poses an additional challenge, as this impact depends on the oceanic spatial and temporal scales considered, on DA methods and on model skills. This highlights the need of validation metrics which allow us to separate scales associated with ocean processes, and this work demonstrates that process-oriented metrics are powerful tools to qualify simulations, identify DA gain, and provide greater understanding of major phenomena.

Finally, observations are also used for validation and qualification, steps which are essential to disentangle the complexity of operational systems and provide confidence in ocean state estimates. It is noteworthy that most operational centers choose to assimilate the maximum of available observations, making independent validations impossible. Further investigations should be carried out to determine the full benefit of observations, from their impacts through assimilation to their impact during qualification as an independent dataset.

Acknowledgments. R. B. was funded by a 1-yr postdoctoral fellowship from Institut de Recherche pour le Développement (IRD) (the French National Research Institute for Sustainable Development) and was hosted at Mercator Ocean International (MOI). F. Gasparin and S. Cravatte are funded by IRD. G. Ruggiero and E. Remy are funded by MOI. This work was supported by the French National program Les Enveloppes Fluides et l'Environnement (LEFE) in the frame of the LEFE/GMMC PODIOM project. This study has been conducted using E.U. Copernicus Marine Service Information. INCOIS Contribution Number 542. We thank two anonymous reviewers whose comments helped to improve this manuscript.

Data availability statement. This study has been conducted using E.U. Copernicus Marine Service Information (https://marine.copernicus.eu). The free version of the GLORYS12 reanalysis can be available on request. Subsurface mooring data were acquired from web archives provided by the TAO Project Office of NOAA/PMEL (www.pmel.noaa.gov/gtmba).

REFERENCES

Ballarotta, M., and Coauthors, 2019: On the resolutions of ocean altimetry maps. *Ocean Sci.*, **15**, 1091–1109, https://doi.org/10.5194/os-15-1091-2019.

Bendat, J. S., and A. G. Piersol, 2010: *Random Data: Analysis and Measurement Procedures*. John Wiley and Sons, 640 pp.

Brasseur, P., and J. Verron, 2006: The SEEK filter method for data assimilation in oceanography: A synthesis. *Ocean Dyn.*, **56**, 650–661, https://doi.org/10.1007/s10236-006-0080-3.

Cabanes, C., and Coauthors, 2013: The CORA dataset: Validation and diagnostics of in-situ ocean temperature and salinity measurements. *Ocean Sci.*, **9** (1), 1–18, https://doi.org/10.5194/os-9-1-2013.

Challenor, P. G., P. Cipollini, and D. Cromwell, 2001: Use of the 3D radon transform to examine the properties of oceanic Rossby waves. *J. Atmos. Oceanic Technol.*, **18**, 1558–1566, https://doi.org/10.1175/1520-0426(2001)018<1558:UOTRTT>2.0.CO;2.

Chelton, D. B., M. G. Schlax, J. M. Lyman, and G. C. Johnson, 2003: Equatorially trapped Rossby waves in the presence of meridionally sheared baroclinic flow in the Pacific Ocean. *Prog. Oceanogr.*, **56**, 323–380, https://doi.org/10.1016/S0079-6611(03)00008-9.

Cravatte, S., J. Picaut, and G. Eldin, 2003: Second and first baroclinic Kelvin modes in the equatorial Pacific at intraseasonal timescales. *J. Geophys. Res.*, **108**, 3266, https://doi.org/10.1029/2002JC001511.

——, W. S. Kessler, N. Smith, and S. E. Wijffels, 2016: First report of TPOS 2020. GOOS Rep.-215, 202 pp., https://tpos2020.org/first-report/.

Dee, D. P., and Coauthors, 2011: The ERA-Interim reanalysis: Configuration and performance of the data assimilation system. *Quart. J. Roy. Meteor. Soc.*, **137**, 553–597, https://doi.org/10.1002/qj.828.

Farrar, J. T., 2008: Observations of the dispersion characteristics and meridional sea level structure of equatorial waves in the Pacific Ocean. *J. Phys. Oceanogr.*, **38**, 1669–1689, https://doi.org/10.1175/2007JPO3890.1.

——, 2011: Barotropic Rossby waves radiating from tropical instability waves in the Pacific Ocean. *J. Phys. Oceanogr.*, **41**, 1160–1181, https://doi.org/10.1175/2011JPO4547.1.

——, and R. A. Weller, 2006: Intraseasonal variability near 10°N in the eastern tropical Pacific Ocean. *J. Geophys. Res.*, **111**, C05015, https://doi.org/10.1029/2005JC002989.

——, and T. S. Durland, 2012: Wavenumber–frequency spectra of inertia–gravity and mixed Rossby–gravity waves in the equatorial Pacific Ocean. *J. Phys. Oceanogr.*, **42**, 1859–1881, https://doi.org/10.1175/JPO-D-11-0235.1.

Fujii, Y., and Coauthors, 2019: Observing system evaluation based on ocean data assimilation and prediction systems: On-going challenges and a future vision for designing and supporting ocean observational networks. *Front. Mar. Sci.*, **6**, 417, https://doi.org/10.3389/fmars.2019.00417.

Gasparin, F., and Coauthors, 2018: A Large-scale view of oceanic variability from 2007 to 2015 in the global high resolution monitoring and forecasting system at Mercator Océan. *J. Mar. Syst.*, **187**, 260–276, https://doi.org/10.1016/j.jmarsys.2018.06.015.

——, J.-M. Lellouche, S. E. Cravatte, G. Ruggiero, B. Rohith, P. Y. Le Traon, and E. Rémy, 2023: On the control of spatial and temporal oceanic scales by existing and future observing systems: An observing system simulation experiment approach. *Front. Mar. Sci.*, **10**, 1021650, https://doi.org/10.3389/fmars.2023.1021650.

Good, S. A., M. J. Martin, and N. A. Rayner, 2013: EN4: Quality controlled ocean temperature and salinity profiles and monthly objective analyses with uncertainty estimates. *J. Geophys. Res. Oceans*, **118**, 6704–6716, https://doi.org/10.1002/2013JC009067.

Gourdeau, L., J. Verron, A. Chaigneau, S. Cravatte, and W. Kessler, 2017: Complementary use of glider data, altimetry, and model for exploring mesoscale eddies in the Tropical Pacific Solomon Sea. *J. Geophys. Res. Oceans*, **122**, 9209–9229, https://doi.org/10.1002/2017JC013116.

Kessler, W. S., M. C. Spillane, M. J. McPhaden, and D. E. Harrison, 1996: Scales of variability in the equatorial Pacific inferred form Tropical Atmosphere-Ocean buoy array. *J. Climate*, **9**, 2999–3024, https://doi.org/10.1175/1520-0442(1996)009<2999:SOVITE>2.0.CO;2.

Lellouche, J.-M., and Coauthors, 2013: Evaluation of global monitoring and forecasting systems at Mercator Océan. *Ocean Sci.*, **9**, 57–81, https://doi.org/10.5194/os-9-57-2013.

——, and Coauthors, 2018: Recent updates to the Copernicus Marine Service global ocean monitoring and forecasting real-time 1/12° high-resolution system. *Ocean Sci.*, **14**, 1093–1126, https://doi.org/10.5194/os-14-1093-2018.

——, and Coauthors, 2021: The Copernicus global 1/12° oceanic and sea ice GLORYS12 reanalysis. *Front. Earth Sci.*, **9**, 698876, https://doi.org/10.3389/feart.2021.698876.

Le Traon, P. Y., and Coauthors, 2019: From observation to information and users: The Copernicus Marine Service perspective. *Front. Mar. Sci.*, **6**, 234, https://doi.org/10.3389/fmars.2019.00234.

Lyman, J. M., D. B. Chelton, R. A. deSzoeke, and R. M. Samelson, 2005: Tropical instability waves as a resonance between equatorial Rossby waves. *J. Phys. Oceanogr.*, **35**, 232–254, https://doi.org/10.1175/JPO-2668.1.

——, G. C. Johnson, and W. S. Kessler, 2007: Distinct 17- and 33-day tropical instability waves in subsurface observations. *J. Phys. Oceanogr.*, **37**, 855–872, https://doi.org/10.1175/JPO3023.1.

Martin, M. J., and Coauthors, 2015: Status and future of data assimilation in operational oceanography. *J. Oper. Oceanogr.*, **8** (suppl.), s28–s48, https://doi.org/10.1080/1755876X.2015.1022055.

McPhaden, M. J., and Coauthors, 1998: The Tropical Ocean-Global Atmosphere observing system: A decade of progress. *J. Geophys. Res.*, **103**, 14 169–14 240, https://doi.org/10.1029/97JC02906.

Melet, A., L. Gourdeau, and J. Verron, 2010: Variability in Solomon Sea circulation derived from altimeter sea level data. *Ocean Dyn.*, **60**, 883–900, https://doi.org/10.1007/s10236-010-0302-6.

Moore, D. W., and S. G. H. Philander, 1977: Modelling the tropical ocean circulation. *The Sea*, E. D. Goldberg et al. Eds., Harvard University Press, 319–361.

NCAR Command Language, 2019: The NCAR command language version 6.6.2. UCAR/NCAR/CISL/TDD, accessed 5 July 2022, https://doi.org/10.5065/D6WD3XH5.

Pujol, M.-I., Y. Faugère, G. Taburet, S. Dupuy, C. Pelloquin, M. Ablain, and N. Picot, 2016: DUACS DT2014: The new multi-mission altimeter data set reprocessed over 20 years. *Ocean Sci.*, **12**, 1067–1090, https://doi.org/10.5194/os-12-1067-2016.

Roundy, P. E., and W. M. Frank, 2004: Effects of low-frequency wave interactions on intraseasonal oscillations. *J. Atmos. Sci.*, **61**, 3025–3040, https://doi.org/10.1175/JAS-3348.1.

Smith, S. R., and Coauthors, 2019: Ship-based contributions to global ocean, weather, and climate observing systems. *Front. Mar. Sci.*, **6**, 434, https://doi.org/10.3389/fmars.2019.00434.

Specht, M. S., J. Jungclaus, and J. Bader, 2024: Seasonality of subsurface shear instabilities at tropical instability wave fronts in the Atlantic Ocean in a high-resolution simulation. *J. Geophys. Res. Oceans*, **129**, e2023JC020041, https://doi.org/10.1029/2023JC020041.

Storto, A., and Coauthors, 2019: Ocean reanalyses: Recent advances and unsolved challenges. *Front. Mar. Sci.*, **6**, 418, https://doi.org/10.3389/fmars.2019.00418.

Szekely, T., J. Gourrion, S. Pouliquen, and G. Reverdin, 2019: The CORA 5.2 dataset for global in situ temperature and salinity measurements: Data description and validation. *Ocean Sci.*, **15**, 1601–1614, https://doi.org/10.5194/os-15-1601-2019.

Wheeler, M., and G. N. Kiladis, 1999: Convectively coupled equatorial waves: Analysis of clouds and temperature in the wavenumber–frequency domain. *J. Atmos. Sci.*, **56**, 374–399, https://doi.org/10.1175/1520-0469(1999)056%3C0374:CCEWAO%3E2.0.CO;2.

Willett, C. S., R. R. Leben, and M. F. Lavín, 2006: Eddies and tropical instability waves in the eastern tropical Pacific: A review. *Prog. Oceanogr.*, **69**, 218–238, https://doi.org/10.1016/j.pocean.2006.03.010.